RSC Advances

ROYAL SOCIETY OF CHEMISTRY

PAPER

View Article Online
View Journal | View Issue

Cite this: *RSC Adv.*, 2025, **15**, 32919

Electric field-assisted annular arrangement of sulfonated polystyrene particles for isotropically enhanced matrix performance

Yajun Zhang, *[ab] Xiangmeng Li, [a] Jinjing Zhang,[c] Chao Yan,[a] Jiaojiao Li[a] and Xijing Zhu[a]

An ordered and rationally designed distribution structure can fully exploit the superior properties of micro/nano-fillers, maximizing the synergistic effects between the fillers and the matrix. However, current research primarily focuses on the linear alignment of fillers, which only enhances the composite's performance along a specific direction. In this study, sulfonated polystyrene (SPS) particles were arranged in an annular pattern induced by an electric field. Similar to the role of aggregates in concrete, the oriented SPS particles acted as rigid support points, constructing "micro-bridges" within the matrix. These SPS particles cooperatively bore the load with the matrix, reducing stress concentration and enabling the composite to exhibit improved integrity and stability. In tensile tests, hydrogels containing 1 wt% oriented particles demonstrated an approximately 68.5% increase in fracture elongation and a 7.67 kPa enhancement in tensile strength compared to the pure polyacrylamide hydrogel. This study introduces a novel filler annular orientation strategy that enables isotropic enhancement of composite properties while effectively overcoming the limitations imposed by conventional direction-dependent reinforcement mechanisms.

Received 9th June 2025
Accepted 7th September 2025

DOI: 10.1039/d5ra04063a

rsc.li/rsc-advances

1. Introduction

In polymer-matrix composites, the incorporation of an optimal amount of micro/nano-fillers can effectively enhance mechanical properties such as strength, modulus, and hardness, while simultaneously improving functional characteristics including thermal stability, electrical conductivity, and thermal conductivity.[1–6] However, the reinforcing efficiency of micro/nano-fillers in composites depends not only on their intrinsic properties and loading content, but also critically on their spatial distribution within the matrix.[7–9] Different filler arrangements directly influence the interfacial interactions between fillers and matrix, stress transfer efficiency, and the degree to which the fillers' inherent properties are utilized.[10–13] Randomly dispersed fillers tend to form agglomerates, which not only reduce the effective utilization of fillers but also induce stress concentration, leading to performance degradation. In contrast, well-organized and rationally designed filler architectures can fully exploit the superior characteristics of micro/nano-fillers, maximize the synergistic effects between fillers and matrices, and consequently further improve the overall performance of composites.[14–16]

The selection of fillers spans diverse categories, including carbon-based materials, inorganic non-metallic compounds, metallic nanoparticles, *etc.*[17–21] For filler arrangement strategies, conventional mechanical blending remains the most prevalent approach, employing vigorous stirring, ball milling, or ultrasonication to disperse fillers within the matrix.[22] However, this method often induces filler agglomeration, limiting precise spatial control and necessitating additional post-processing such as mechanical stretching for optimized distribution.[23–25] The solution-based method facilitates uniform dispersion of fillers through solvent mediation, followed by composite formation *via* solvent evaporation and solidification.[26–28] Although this approach improves filler distribution to some extent, structural defects such as shrinkage, porosity, or filler aggregation often arise during solvent removal, ultimately compromising mechanical performance. The template-assisted strategy achieves controlled filler localization by exploiting pore channels and surface features of the templates, facilitating large-area, periodic filler organization.[29–31] However, the fabrication of high-precision templates typically requires costly and time-intensive processing. External fields have emerged as a powerful and versatile approach to achieving controlled alignment of micro/nano-fillers in composite materials.[32] Commonly employed fields include magnetic,[33–38] electric,[39–43] and acoustic fields. Field-assisted techniques enable non-

---

[a] Shanxi Provincial Key Laboratory for Advanced Manufacturing Technology, North University of China, Taiyuan 030051, China. E-mail: yajunzhang@nuc.edu.cn
[b] State Key Laboratory for Manufacturing Systems Engineering, Xi'an Jiaotong University, Xi'an 710054, China
[c] School of Logistics, Beijing Wuzi University, Beijing 101149, China

contact, energy-efficient, and spatially programmable manipulation of filler orientation.

However, most studies on filler-reinforced composites have relied on linear alignment of the fillers, yielding high strength and modulus along a specific direction while simultaneously introducing mechanical weakness in all other orientations.[44–46] In recent years, "mechanical isotropization" has become a central topic in lightweight composite research. In two-dimensional systems, Cheng and colleagues fabricated $Ti_3C_2T_x$/graphene hybrid films *via* π–π crosslinking at room temperature; the resulting nanocomposites exhibited tensile strengths of 1.87 GPa and Young's moduli of 98.7 GPa; these sheets demonstrated an isotropic in-plane room temperature electrical conductivity of up to 1423 S cm^{-1}.[47] Additive manufacturing and sheet-moulding compound (SMC) technologies have further expanded manufacturability. Xiang *et al.* combined 30 mm chopped carbon fibres with vacuum hot-pressed SMC to produce carbon fiber reinforced polymer (CFRP) panels. The CFRP composites with 25–30% vol carbon fibers have 2% dispersion coefficient of tensile strength in various directions.[48]

The performance ceiling of modern polymer–matrix composites is no longer dictated solely by the intrinsic properties of the matrix; rather, it is increasingly set by the judicious selection and interfacial engineering of secondary fillers. In the present study, sulfonated polystyrene (SPS) particles were chosen as reinforcing fillers on account of their distinctive physicochemical characteristics. The advantages of SPS particles can be summarized as follows: (I) Facile surface engineering and functionalization: The $-SO_3H$ layer acts as a reactive anchor for covalent attachment of amines, thiols, or metal nanoparticles (Ag, Fe_3O_4).[49] (II) Outstanding colloidal dispersibility and interfacial activity: SPS particles possess ζ-potentials as high as −55 mV, ensuring stable dispersions in aqueous media and spontaneous assembly at oil/water interfaces.[50] (III) Scalable synthesis and monodispersity: Emulsifier-free or seeded-swelling polymerization yields uniform micro- and nano-spheres amenable to continuous-flow processing and industrial scale-up.[51] Collectively, these attributes position SPS particles as multifunctional platforms for catalysis, environmental remediation, and advanced composite materials.

Conventionally chemically cross-linked hydrogels exhibit the archetypal "soft-yet-brittle" signature under swollen conditions, rendering them inadequate for tissue-engineering scaffolds or flexible electronics that require simultaneous high-load bearing and fatigue resistance. In this study, a nanocomposite-toughening strategy was proposed in which SPS particles were assembled into concentric ring patterns within the polyacrylamide (PAAm) matrix, leading to an isotropic enhancement of the hydrogel's mechanical performance. Specifically, a high-frequency alternating-current (AC) signal of 400 V_{p-p} and 1 MHz was applied to cylindrical electrodes, and within approximately 6 seconds, the SPS particles formed an annular arrangement. The matrix solution was then photopolymerized *via* UV irradiation, permanently fixing the particle arrangement within the matrix. As illustrated in Fig. 1, the SPS particles created an annular topological network within the matrix and formed hydrogen bonds with adjacent PAAm molecular chains. These interactions effectively established new crosslinking points, modified the original gel network microstructure, and tightened interchain connections. Under external stress, forces were uniformly distributed along the ring-like topology *via* these crosslinks, significantly improving deformation resistance. Our work introduced an annular arrangement of spherical particles that provided isotropic enhancement to the material, effectively eliminating directional limitations. This composite strategy showed great promise for applications requiring high mechanical strength and biocompatibility, such as tissue-engineering scaffolds and drug-delivery carriers.

2. Experimental section

2.1. Materials

Polystyrene (PS) particles with diameters of 300 nm and 3 μm were commercially obtained from Yiyuan Biotechnology Co., Ltd (Shanghai, China). The precursor solution was formulated with 1 wt% particles in an aqueous phase containing 40 wt% acrylamide monomer (AAm, 99% purity). The crosslinker was

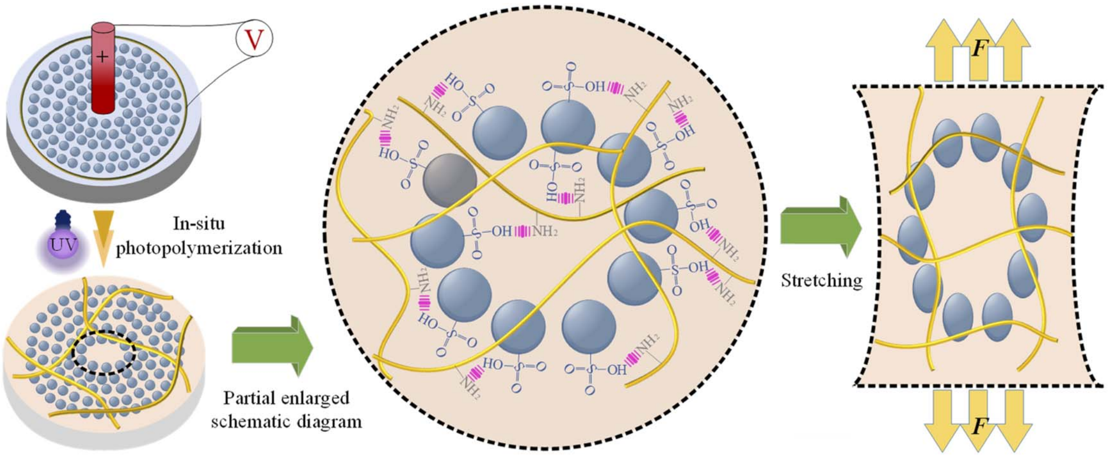

Fig. 1 The annular arrangement structure of SPS particles that provide isotropic reinforcement to the matrix.

N,*N*′-methylenebisacrylamide (MBAA, 99% purity). The mass ratio of monomer to crosslinker was kept at 200 : 1. The photoinitiator was Irgacure 2959, with an added amount of 0.1 wt%. The monomer, crosslinker and photoinitiator were all purchased from Sigma-Aldrich Trade Co., Ltd (Shanghai, China).

2.2. Preparation of SPS/PAAm composites

An AC sinusoidal signal (400 V_{p-p}, 1 MHz) was provided by using a waveform generator (Unit UTG2062A) and a high-voltage amplifier (Aigtek, ATA-2048). The output electrical signal was applied to a copper electrode column with a diameter of 200 μm and a length of 5 mm, as shown in Fig. 2. After the electric field was applied for about 6 seconds, the SPS particles in the solution gradually assumed an annular arrangement. The solution was illuminated with ultraviolet light at a wavelength of 365 nm for 3 minutes. Driven by the photoinitiator and specific wavelength light source, the liquid acrylamide monomers underwent a chain reaction and rapidly cross-linked to form a solid polyacrylamide network. After the curing process was completed, the resulting SPS/PAAm composite was demoulded and rinsed with deionized water to remove unreacted monomers.

2.3. Sulfonation of polystyrene particles

Sulfuric acid (98% concentration, 60 mL) was added to a flask that contained polystyrene particle powder (2.0 g). The mixture was dispersed using ultrasonication at 50 °C for 10 hours. Ultrasonication helped to break up any aggregates and ensured a more uniform reaction by creating cavitation bubbles in the liquid, which could help in the dispersion of the PS particles. After the reaction was complete, the mixture was neutralized with concentrated potassium hydroxide (KOH) solution. This step was crucial to neutralize any remaining acid. The mixture was then poured into a sintered glass funnel, which allowed for the separation of the solid SPS particles from the liquid. The SPS particles were thoroughly washed with distilled water to remove any by-products, unreacted starting materials, or neutralization agents. Finally, the SPS particles were vacuum-dried at 50 °C until they reached a constant weight. Vacuum-drying helped to remove any remaining water or solvent from the particles, which was important for their stability and to ensure accurate weight measurements. This process resulted in SPS particles that had sulfonic acid groups attached to the polystyrene backbone, as shown in Fig. 3.

2.4. Characterization

The morphology and microstructure of the samples were visualized and analyzed using a scanning electron microscope (SEM, Hitachi 8100). The thermal stability of the hydrogels was analyzed by a thermogravimetric analyzer (Discovery TGA 5500). In addition, the mechanical properties were evaluated using a universal testing machine (INSTRON 5944), enabling the quantification of parameters such as tensile strength, stiffness, and toughness. To study the swelling behavior of the hydrogels, they were freeze-dried using a freeze dryer (LGJ-12D, China). The resulting lyophilized samples were then completely immersed in deionized water at 23 °C. To monitor the swelling process over time, the samples were weighed every 10 hours until they reached a constant weight. The swelling ratio (SR) of

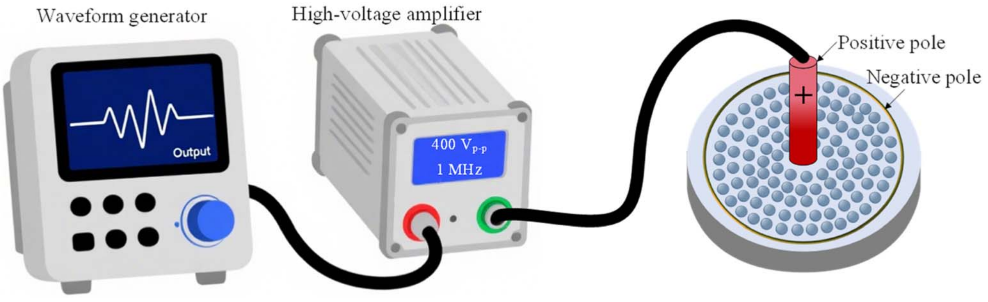

Fig. 2 Schematic diagram of the electric field setup.

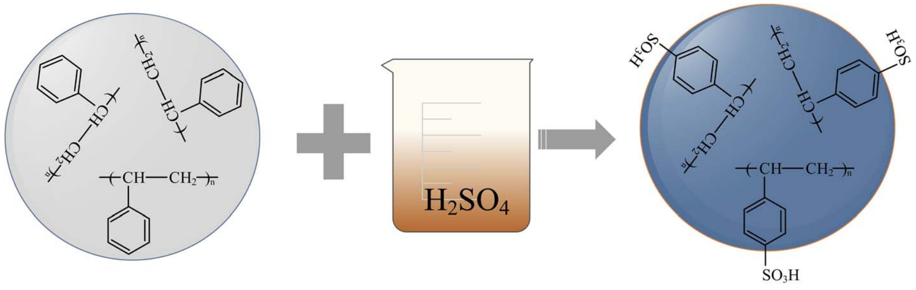

Fig. 3 The schematic diagram of sulfonation mechanism of PS particles.

the hydrogels was calculated according to the following formula:

$$\mathrm{SR} = \frac{W_t - W_0}{W_0} \tag{1}$$

where W_t is the weight of swollen hydrogels at time t, and W_0 is the weight of lyophilized hydrogels. The deswelling ratio (DSR) of hydrogels was calculated by the following formula:

$$\mathrm{DSR} = \frac{W_t - W_0}{W_\mathrm{d} - W_0} \tag{2}$$

where W_d is the initial weight of swollen hydrogels.

3. Results and discussion

3.1. Sulfonation characterization of SPS particles

Fig. 4 presented the SEM images of PS and SPS particles. The pristine PS particles (Fig. 4a and b) exhibited a smooth and uniformly spherical morphology. In contrast, SPS particles (Fig. 4c and d) displayed a distinctly rough and fractured surface structure, resulting from sulfuric acid-induced corrosion that generated extensive cracking. Upon drying, these surface cracks created an irregular, strawberry-like texture on the SPS particles. Notably, the sulfonation process did not substantially alter the particle sizes, and the modified particles maintained excellent dispersibility despite their altered surface morphology.

Energy dispersive spectroscopy (EDS) was employed to analyze the surface elemental distribution of particles, verifying the success of the sulfonation process. EDS line scanning was performed by directing an electron beam across the sample, generating an elemental distribution profile along a defined path. As illustrated in Fig. 5, the EDS line scan results revealed distinct sulfur (S) signals in SPS particles, confirming effective sulfonation. Both the pristine PS and SPS samples exhibited platinum (Pt) signals, which resulted from the conductive Pt coating applied prior to EDS analysis to enhance sample conductivity and imaging quality. The relative quantitative information of C, O, and S elements in SPS particles determined by EDS was shown in Table 1.

3.2. Simulation analysis

When SPS particles were subjected to a non-uniform electric field, surface polarization charges were induced on the particles. These charges arose from the dielectric polarization of molecules under the applied electric field. In this study, a 3D polarization model of SPS particles in a non-uniform electric field was developed using COMSOL Multiphysics, as illustrated in Fig. 6a. When opposite voltages of ± 10 V were applied to the upper and lower electrode plates, the polarization intensity of SPS particles on the side of the smaller electrode plate was higher than that on the larger electrode plate side, as illustrated in Fig. 6b. Polarization intensity, which quantified the degree of charge separation in a dielectric medium, was directly proportional to the electric field intensity. Thus, a stronger electric field induced greater polarization in the medium. An electric field was generated using a cylindrical electrode, with an applied voltage of 200 V. The resulting electric field distribution

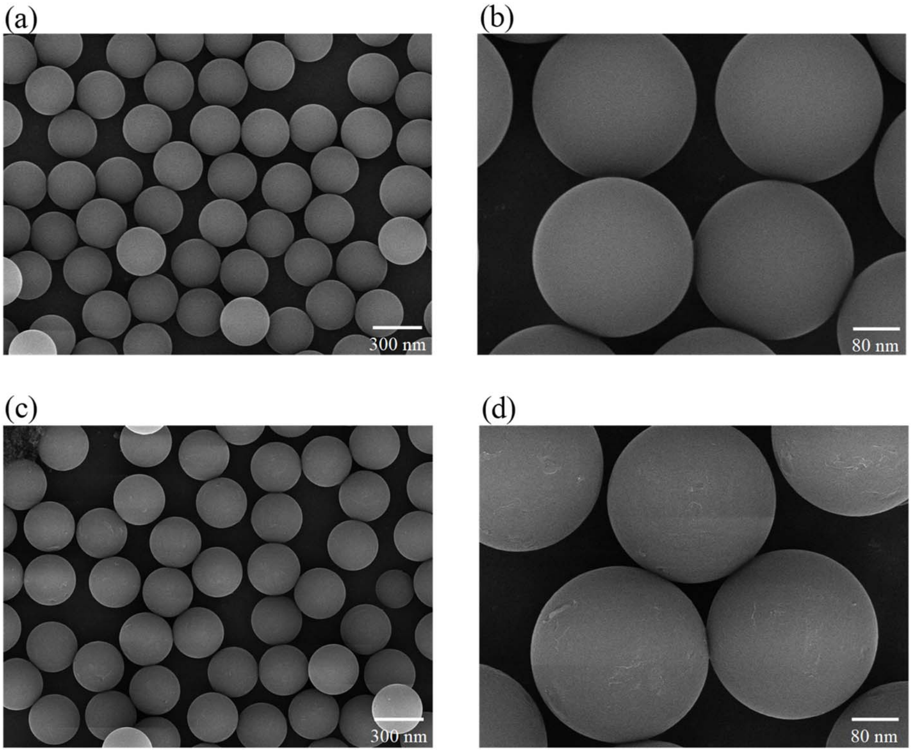

Fig. 4 Sulfonation characterization of SPS particles. (a) and (b) SEM images of PS particles with smooth and uniform spherical morphology. (c) and (d) SEM images of SPS particles with the distinctly rough and fractured surface structure.

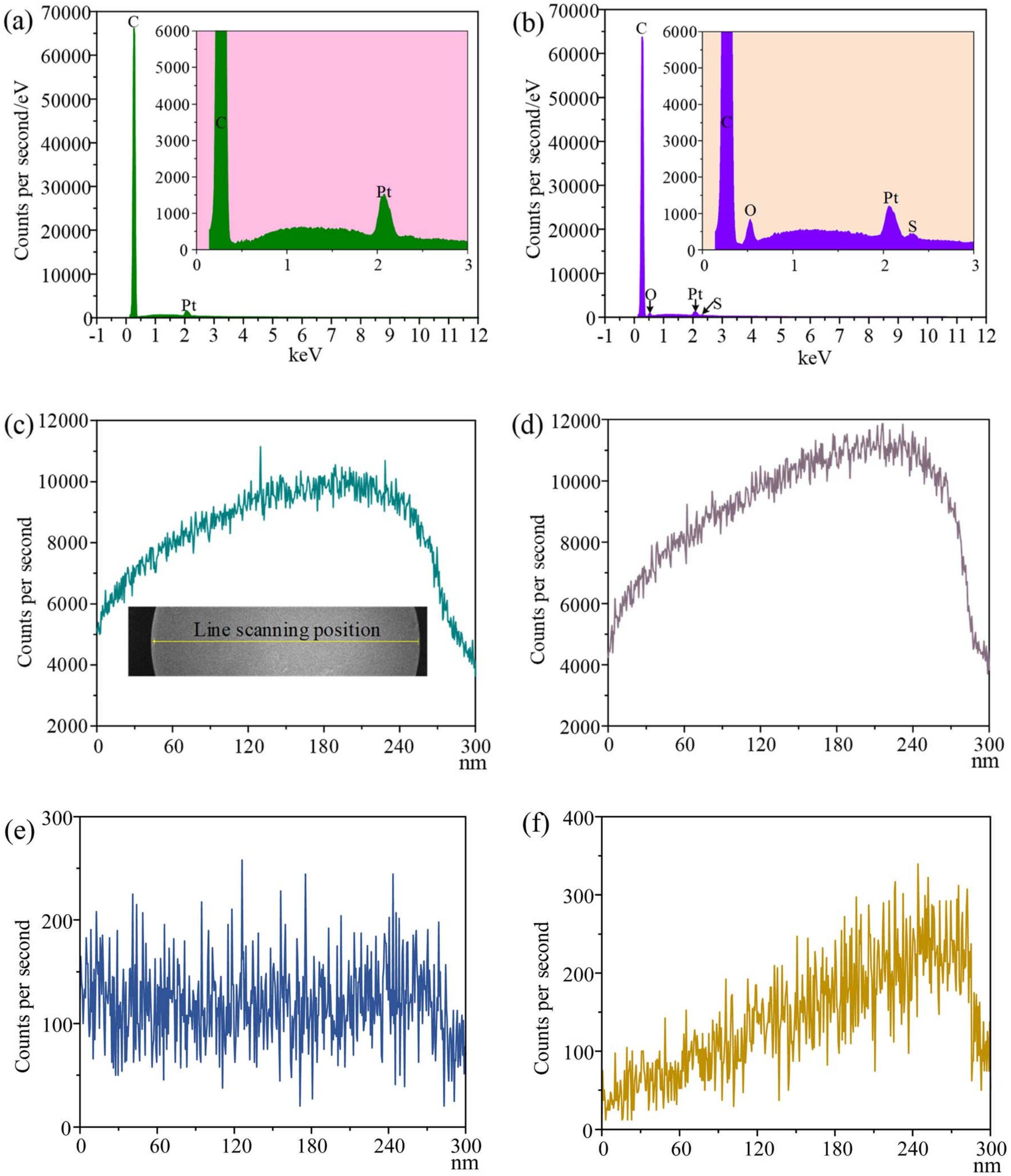

Fig. 5 The surface elemental distribution of particles. (a) Line sum spectrum of PS particles. (b) Line sum spectrum of SPS particles. (c) Line spectrum of C element in PS particles. (d) Line spectrum of C element in SPS particles. (e) Line spectrum of S element in SPS particles. (f) Line spectrum of O element in SPS particles.

Table 1 The relative quantitative information of C, O, and S elements in SPS particles

Elements	Atomic content (%)	Standard deviation
C	96.6	0.15
O	3.05	0.11
S	0.35	0.02

was shown in Fig. 6c. The field direction, represented by conical arrows, radiated outward from the cylindrical electrode's edge. The size of the arrows indicated the field intensity, with larger cones corresponding to stronger fields near the electrode. The maximum electric field intensity in this region reached approximately 10^5 V m^{-1}.

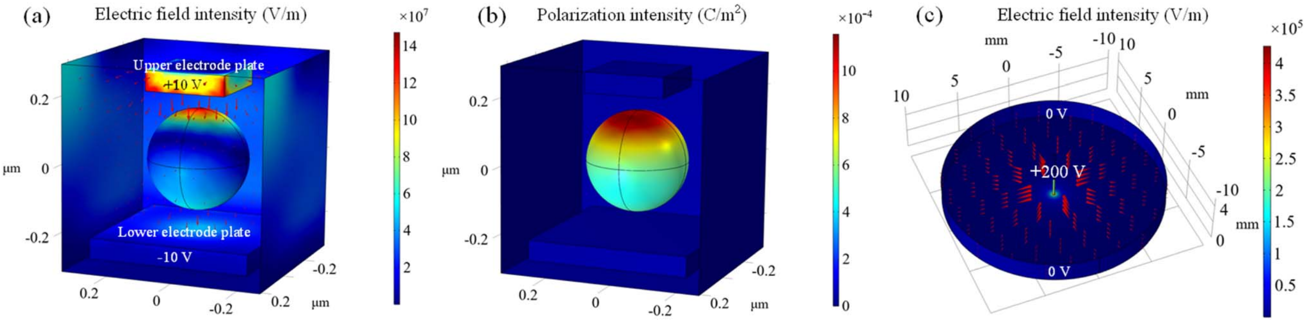

Fig. 6 Simulation Analysis. (a) The 3D polarization model of SPS particles in a non-uniform electric field. (b) The polarization intensity of SPS particles. (c) Electric field intensity around a cylindrical electrode.

3.3. The annular arrangement of SPS particles

The primary forces acting on particles in an electric field are dielectrophoretic (DEP) force, inertial force, and Stokes drag force. The dielectrophoretic force (F_d) serves as the driving force that promotes particle motion, while the Stokes drag force (F_s) acts as a viscous resistance that hinders particle movement. The inertial force (F_i) is the resultant force of the buoyant force (F_b) and the gravitational force (F_g) acting on the particle. According to Newton's second law, the net external force (F_e) on a particle can be expressed as:

$$F_e = F_d + F_s + F_i = m_p \frac{dv_p}{dt} \tag{3}$$

v_p represents the particle velocity.

Buoyancy and gravity act in the vertical plane and determine the suspension state of the particles in the fluid. Consequently, the inertial force can be expressed as follows:

$$F_i = F_b - F_g = \frac{4}{3}\pi r^3 g(\rho_m - \rho_p) \tag{4}$$

r is the radius of the particles; ρ_m is the density of the matrix solution; and ρ_p is the density of the particles.

If the viscosity of the matrix solution is relatively high, its influence on the motion of the particles cannot be neglected and will impede their movement. This force is known as Stokes drag, expressed as follows:

$$F_d = 6\pi\eta r_p(v_f - v_p) \tag{5}$$

η is the viscosity of the solution; v_f is the fluid flow velocity; v_p is the particle velocity.

The force of electric field on particles is called dielectrophoresis force, and it is defined as follows:

$$F_d = 2\pi\varepsilon_m r^3 \mathrm{Re}[f_{CM}]\nabla|E|^2 \tag{6}$$

where ε_m is the absolute permittivity of the medium; r is the radius of spherical particle; E is the field intensity; $\nabla|E|^2$ is the square of the electric field gradient; f_{CM} is the Clausius–Mossotti factor; Re[f_{CM}] is the real part of f_{CM}, and f_{CM} is defined as follows:

$$f_{CM} = \frac{\varepsilon_p^* - \varepsilon_m^*}{\varepsilon_p^* + 2\varepsilon_m^*} \tag{7}$$

ε_p^* and ε_m^* are the complex permittivities of the particle and the medium respectively, and ε^* is expressed by its permittivity ε and conductivity σ:

$$\varepsilon^* = \varepsilon - i\frac{\sigma}{\omega} \tag{8}$$

where $\omega = 2\pi f$, is the angular frequency of the electric field, and f is the frequency. The direction of DEP force depends on permittivities and conductivities of medium and particles. If Re[f_{CM}] > 0, the particles will be subjected to positive DEP force. If Re[f_{CM}] < 0, the particles will be subjected to negative DEP force. Calculations showed that, at an electric-field frequency of 1 MHz, SPS particles experienced a negative DEP force. This force drove the particles toward regions of lower field strength; in a cylindrical-electrode configuration it therefore pushed them away from the electrode posts. As shown in Fig. 7a and b, simulations predicted that the particles would ultimately be repelled to the outermost periphery, where they formed a continuous annular aggregate. Experimental realization of this terminal pattern, however, required field application times exceeding 10 min. Such prolonged exposure generated excessive Joule heating that caused the matrix solution to evaporate completely. Interestingly, during the transient phase preceding the terminal state, the particles spontaneously organized into a transient annulus within 6 seconds. As shown in Fig. 7c and d, this intermediate configuration was captured *via* optical microscope. The transient annular arrangement was subsequently immobilized by *in situ* photopolymerization of the matrix solution, resulting in SPS/PAAm composite materials. Where local particle concentration was high, neighboring particles assembled into chains under the combined action of the local field gradient and dipole–dipole attraction (Fig. 7e and f).

3.4. Swelling and deswelling behavior of hydrogels

The swelling ratio of hydrogels over time at 23 °C was shown in Fig. 8a. The hydrogel began to absorb water when it was first exposed. This initial phase (0–20 h) was characterized by a rapid increase in the volume of the hydrogel as it took up water. As time progressed, the rate of water absorption slowed down. This was because the hydrogel's internal structure started to resist further swelling due to the balance between the osmotic pressure (which drove water into the hydrogel) and the elastic forces

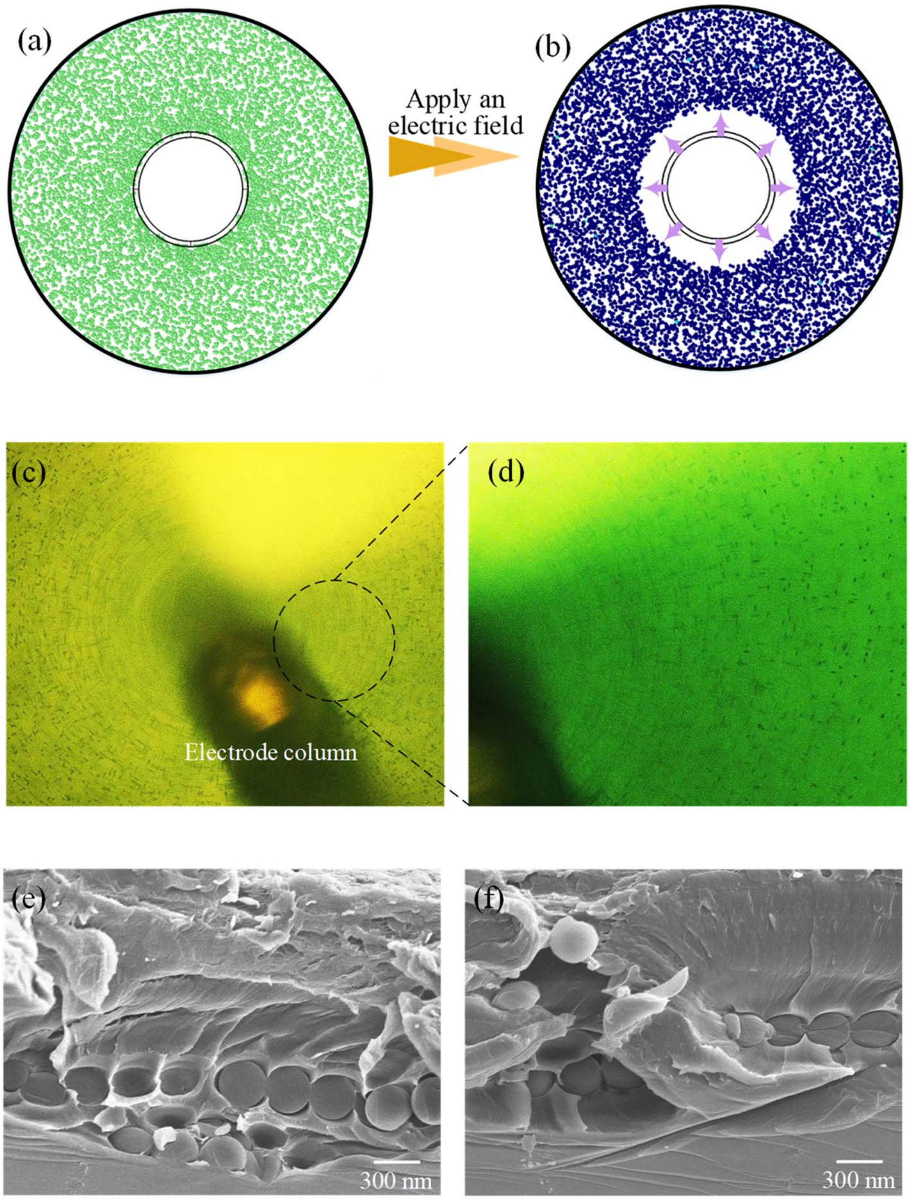

Fig. 7 (a) The particle distribution before motion initiation in simulation. (b) The motion trend of particles in simulation (c) The arrangement of SPS particles under a cylindrical electrode in the experiment. (d) Partial enlarged view of the particle arrangement state. (e) and (f) Chains assembled from adjacent particles observed under SEM.

within the hydrogel network (which resisted the expansion). The deswelling kinetics of hydrogels were investigated over a 80 hours period at 37 °C (Fig. 8b). The deswelling ratio, expressed as a percentage of the initial swollen state, was plotted against time to evaluate the water retention capacity and structural stability of the hydrogels. The deswelling ratio was highest in the first 10 hours, followed by a slower decline, and eventually approached a plateau. Particle orientation significantly influenced the swelling and deswelling behavior of hydrogels, which could be primarily attributed to the following aspects: (I) The sulfonic acid groups ($-SO_3H$) on the surface of SPS particles formed hydrogen bonds with the amide groups ($-CONH_2$) of the PAAm chains, leading to an increase in effective crosslinking density and a reduction in network pore size, thereby restricting water penetration. (II) SPS particles exhibited a steric hindrance effect, acting as physical barriers that impeded the extension of polymer chains during swelling or suppressed structural collapse during deswelling. (III) The interfacial energy effect required water molecules to overcome an additional energy barrier at the SPS/PAAm interface, resulting in reduced water absorption/desorption rates.

3.5. Mechanical properties of hydrogels

Notably, the hydrogel exhibited relatively outstanding mechanical properties. After undergoing deformations such as puncture (Fig. 8d) and stretching (Fig. 8e), the hydrogel could

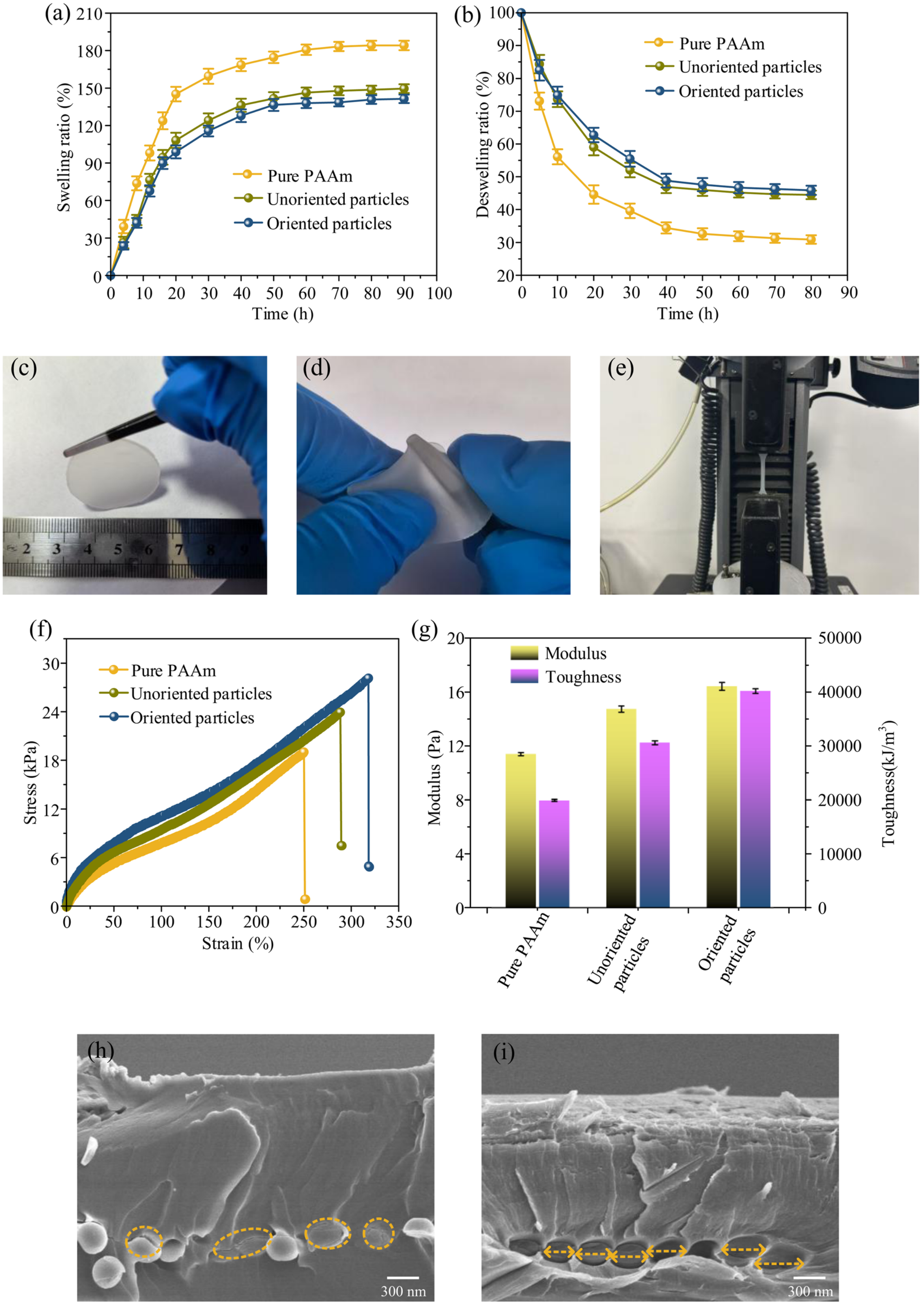

Fig. 8 (a) The swelling ratio of hydrogels over time at 23 °C. (b) The deswelling ratio of hydrogels over a 80 hours period at 37 °C, where the error bars represent the standard deviation obtained from five independent repeated experiments. (c) The SPS/PAAm composite hydrogel. (d) Puncture resistance of the SPS/PAAm composite hydrogel. (e) The stretched SPS/PAAm composite hydrogel. (f) Tensile strain–stress curves of hydrogels. (g) The calculated modulus and toughness of hydrogels derived from strain–stress curves. (h) Particle breakage. (i) Particle deformation along the stretching direction.

still maintain its structural integrity. Fig. 8f illustrated the strain–stress curve of hydrogels. Compared to pure PAAm hydrogel, the fracture elongation and tensile strength of the hydrogel containing oriented particles increased by approximately 68.5% and 7.67 kPa, respectively. The stiffness of materials is typically characterized by Young's modulus, which is defined as:

$$E = \frac{\sigma}{\varepsilon} \tag{9}$$

where E represents Young's modulus, σ denotes stress, and ε signifies strain. The area under the strain–stress curve corresponds to the energy absorbed by the material before fracture, namely the toughness value. Fig. 8g displayed the calculated modulus and toughness of hydrogels derived from strain–stress curves. The incorporation of SPS particles as rigid fillers enhanced the mechanical properties of hydrogels, which could be attributed to the following mechanisms: (I) The SPS particles functioned as multifunctional crosslinking points, increasing the network density of hybrid hydrogels. Under external forces, energy dissipation occurred more uniformly through the crosslinked network, thereby improving deformation resistance. (II) During stretching, the polyacrylamide molecular chains underwent orientation along the tensile direction. When stress propagated through the chains and reached the particles, it induced particle breakage or particle deformation that additionally dissipated energy, as shown in Fig. 8h and i. (III) Well-aligned particles played a pivotal role in impeding crack advancement. These particles acted as "barriers" that deflected crack paths, thereby increasing energy consumption during crack propagation and effectively preventing rapid crack extension, ultimately enhancing the fracture toughness of the material.

4. Conclusion

Herein, we report a novel strategy for enhancing the comprehensive performance of PAAm hydrogels. The key findings and innovations of this study are summarized as follows: (I) In contrast to the conventional linear alignment of fillers reported in most previous studies,[2,34,52,53] our approach enables the annular arrangement configuration of fillers within the matrix. This unique arrangement facilitates isotropic enhancement of composite properties. (II) The hydrogen-bond crosslinking between SPS particles and PAAm matrix enhances network rigidity. Under external loading, the particles efficiently transfer stress, primarily attributed to the optimized synergistic load-bearing mechanism between particles and matrix. Importantly, the method proposed in this study has broad applicability and effectively overcomes the limitations imposed by conventional direction-dependent reinforcement mechanisms. Moreover, this technology has shown certain potential in customizing the properties of composite materials by controlling the composition of fillers and matrices, and is expected to be widely applied in flexible electronic products, biomedical and other fields.

Conflicts of interest

There are no conflicts to declare.

Data availability

The data supporting the findings of this study are included in the article.

Acknowledgements

This work was supported by the National Natural Science Foundation of China (No. 62404208), the Postdoctoral Fellowship Program of China Postdoctoral Science Foundation (No. GZC20241581), the China Postdoctoral Science Foundation (No. 2024M752993), the Opening Foundation of Shanxi Provincial Key Laboratory for Advanced Manufacturing Technology (No. XJZZ202403), the Opening Foundation of State Key Laboratory for Manufacturing Systems Engineering (No. sklms2024002), Aeronautical Science Foundation of China (No. 2023Z0560U0001), Research Project Supported by Shanxi Province Science and Technology Cooperation and Exchange Special Project (No. 202204041101006), Research Project Supported by Shanxi Scholarship Council of China (No. 2023-130), the Opening Projects of State Key Laboratory of Special Vehicle Design and Manufacturing Integration Technology (No. GZ2023KF013).

References

1 Z. Guo, W. Li, H. Wu, L. Cao, S. Song, X. Ma, J. Shi, Y. Ren, T. Huang, Y. Li and Z. Jiang, *Nat. Commun.*, 2025, **16**, 3617.
2 A. J. Chandran, S. M. Rangappa, I. Suyambulingam and S. Siengchin, *J. Vinyl Addit. Technol.*, 2024, **30**, 1083–1123.
3 C. Zheng, J. Yu, X. Li, J. Duan, Z. Huang, M. Li, X. Hu and Y. Li, *J. Mater. Res. Technol.*, 2025, **36**, 4547–4556.
4 W. Yang, Y. S. Zhao, Y. Chen, J. Qiao, W. J. Chen, K. Wang, C. Zhang, J. Zhang, X. Chen and B. Du, *Polym. Compos.*, 2024, **45**, 2749–2758.
5 X. Y. Liu, W. B. Li, Y. J. Jiang, N. Y. Ning and M. Tian, *J. Mater. Chem. A*, 2024, **12**, 9232–9240.
6 M. H. Malakooti, F. Julé and H. A. Sodano, *ACS Appl. Mater. Interfaces*, 2018, **10**, 38359–38367.
7 Y. J. Zhou, R. Ciarla, A. Boonkird, S. Raza, T. Nguyen, J. W. Zhou, N. C. Osti, E. Mamontov, Z. Jiang, X. B. Zuo, J. Ranasinghe, W. G. Hu, B. Scott, J. H. Chen, D. K. Hensley, S. X. Huang, J. Liu, M. D. Li and Y. F. Xu, *Sci. Adv.*, 2025, **11**, eadp6516.
8 Q. G. Chen, K. L. Yang, Y. Feng, L. Liang, M. H. Chi, Z. H. Zhang and X. S. Chen, *Composites, Part A*, 2024, **178**, 107998.
9 C. Harito, D. V. Bavykin, B. Yuliarto, H. K. Dipojono and F. C. Walsh, *NANOSCALE*, 2019, **11**, 4653–4682.
10 K. L. Zhang, C. Chen, Y. F. Wen, X. X. Xu, H. Ni, W. W. Lei, X. M. Ren, J. You, Q. C. Zhang and D. Shi, *Compos. Sci. Technol.*, 2024, **254**, 110666.

11 J. Li, T. Guan, Z. X. Zhang, Y. T. Fu, F. L. Guo, P. Huang, Z. L. Li, Y. Q. Li and S. Y. Fu, *Prog. Mater. Sci.*, 2025, **148**, 101360.

12 J. Wang, J. J. Li, G. J. Weng and Y. Su, *Acta Mater.*, 2020, **185**, 461–473.

13 Y. L. Li, D. Y. Song, Y. Tian, H. Liu, Y. J. Zheng, Y. C. Jia and H. J. Zheng, *Surf. Interfaces*, 2024, **52**, 104908.

14 K. Kim and J. Kim, *Composites, Part B*, 2016, **93**, 67–74.

15 A. Griffin, Y. H. Guo, Z. D. Hu, J. M. Zhang, Y. W. Chen and Z. Qiang, *Polym. Compos.*, 2022, **43**, 5747–5766.

16 C. Y. Kim, T. M. L. Dang, Y. R. N. Zhang, J. F. Yang and B. Wang, *J. Mater.*, 2019, **5**, 679–687.

17 Y. Yao, X. Zhu, X. Zeng, R. Sun, J.-B. Xu and C.-P. Wong, *ACS Appl. Mater. Interfaces*, 2018, **10**, 9669–9678.

18 J. Yang, X. Li, S. Han, R. Yang, P. Min and Z.-Z. Yu, *J. Mater. Chem. A*, 2018, **6**, 5880–5886.

19 P. Lv, X.-W. Tan, K.-H. Yu, R.-L. Zheng, J.-J. Zheng and W. Wei, *Carbon*, 2016, **99**, 222–228.

20 M. Roman and W. T. Winter, *Biomacromolecules*, 2004, **5**, 1671.

21 Y. Li, J. Hong, J. Zhang, H. Yang, H. Wang, L. Ye and Y. Li, *Composites, Part B*, 2025, **289**, 111935.

22 M. Chang, Z. Su and E. Egap, *Macromolecules*, 2016, **49**, 9449–9456.

23 X. Zhao, C. Zhou, Y. Lvov and M. Liu, *Small*, 2019, **15**, 1900357.

24 S. Vowinkel, G. Schaefer, G. Cherkashinin, C. Fasel, F. Roth, N. Liu, C. Dietz, E. Ionescu and M. Gallei, *J. Mater. Chem. C*, 2016, **4**, 3976–3986.

25 D. Mani, M. C. Vu, C.-S. Lim, J.-B. Kim, T.-H. Jeong, H. J. Kim, M. A. Islam, J.-H. Lim, K.-M. Kim and S.-R. Kim, *Carbon*, 2023, **201**, 568–576.

26 S. Panda and S. K. K. Pasha, *Langmuir*, 2023, **39**, 13345–13358.

27 S. P. Espíndola, B. Norder, K. M. B. Jansen, J. Zlopasa and S. J. Picken, *Macromolecules*, 2023, **56**, 9839–9852.

28 S. Wang, B. Yang, L. He, Y. Yang, S. Cui, S. Liu, P. Chen, R. Xia, J. Qian, Y. Ke and T. Jiang, *ACS Appl. Polym. Mater.*, 2023, **5**, 6795–6807.

29 Y. Yao, J. Sun, X. Zeng, R. Sun, J.-B. Xu and C.-P. Wong, *Small*, 2018, **14**, 1704044.

30 X. Zeng, Y. Yao, Z. Gong, F. Wang, R. Sun, J. Xu and C.-P. Wong, *Small*, 2015, **11**, 6205–6213.

31 D. Pan, G. Yang, H. M. Abo-Dief, J. Dong, F. Su, C. Liu, Y. Li, B. B. Xu, V. Murugadoss, N. Naik, S. M. El-Bahy, Z. M. El-Bahy, M. Huang and Z. Guo, *Nano-Micro Lett.*, 2022, **14**, 118.

32 Z. Y. Lin, Y. Liu, S. Raghavan, K. S. Moon, S. K. Sitaraman and C. P. Wong, *ACS Appl. Mater. Interfaces*, 2013, **5**, 7633–7640.

33 S. H. Chung, H. Kim and S. W. Jeong, *Carbon*, 2018, **140**, 24–29.

34 S. H. Chung, J. T. Kim, J. Kim and D. H. Kim, *J. Alloys Compd.*, 2024, **1009**, 176888.

35 K. Kim and J. Kim, *Int. J. Therm. Sci.*, 2016, **100**, 29–36.

36 R. Tognato, A. R. Armiento, V. Bonfrate, R. Levato, J. Malda, M. Alini, D. Eglin, G. Giancane and T. Serra, *Adv. Funct. Mater.*, 2019, **29**, 1804647.

37 X. Guo, S. Cheng, B. Yan, Y. Li, Y. Zhou, W. Cai, Y. Zhang and X.-A. Zhang, *Nano Res.*, 2023, **16**, 2572–2578.

38 M. Ralphs, W. Kong, R. Y. Wang and K. Rykaczewski, *Adv. Mater. Interfaces*, 2019, **6**, 1801857.

39 M. S. Masraff, A. Rahman, M. R. Ramli, M. K. M. Jamil, M. K. Abdullah, M. Z. Ali and Z. Ahmad, *Compos. Sci. Technol.*, 2021, **203**, 108611.

40 J. Lu, X. Ming, M. Cao, Y. Liu, B. Wang, H. Shi, Y. Hao, P. Zhang, K. Li, L. Wang, P. Li, W. Gao, S. Cai, B. Sun, Z.-Z. Yu, Z. Xu and C. Gao, *ACS Nano*, 2024, **18**, 18560–18571.

41 W. Wu, T. Ren, X. Liu, R. Davis, K. Huai, X. Cui, H. Wei, J. Hu, Y. Xia, S. Huang, Z. Qiang, K. Fu, J. Zhang and Y. Chen, *Compos. Commun.*, 2022, **35**, 101309.

42 T. Ji, Y. Feng, M. Qin, S. Li, F. Zhang, F. Lv and W. Feng, *Carbon*, 2018, **131**, 149–159.

43 F. Krisnadi, L. L. Nguyen, Ankit, J. Ma, M. R. Kulkarni, N. Mathews and M. D. Dickey, *Adv. Mater.*, 2020, **32**, 2001642.

44 T. Yoshitomi, T. Matsumoto and T. Nishino, *ACS Appl. Polym. Mater.*, 2023, **5**, 8349–8358.

45 M. Xu, D. N. Futaba, M. Yumura and K. Hata, *ACS Nano*, 2012, **6**, 5837–5844.

46 L. Liu, L. Han, T. Chen, J. Li, Z. Qian and G. Gan, *Langmuir*, 2024, **40**, 20090–20100.

47 J. Yang, M. Li, S. Fang, Y. Wang, H. He, C. Wang, Z. Zhang, B. Yuan, L. Jiang, R. H. Baughman and Q. Cheng, *Science*, 2024, **383**, 771–777.

48 Y.-X. Xiang, K. Shen, H. Wu, Z.-C. He and X.-K. Li, *New Carbon Mater.*, 2021, **36**, 1188–1194.

49 M. Bartel, K. Markowska, M. Strawski, K. Wolska and M. Mazur, *Beilstein J. Nanotechnol.*, 2020, **11**, 620–630.

50 A. Mikkelsen, J. Wojciechowski, M. Rajňák, J. Kurimský, K. Khobaib, A. Kertmen and Z. Rozynek, *Materials*, 2017, **10**, 329.

51 M. Yang, Y. G. Guo, Q. Wu, Y. Luan and G. Wang, *Polymer*, 2014, **55**, 1948–1954.

52 H. Shi, H. Wang, H. Lu, X. Zhang and Z. Zhang, *Langmuir*, 2021, **37**, 8222–8231.

53 Y. Zhang, C. Yan, J. Li, X. Li, Y. Wang, X. Liu and X. Zhu, *J. Colloid Interface Sci.*, 2024, **662**, 1063–1074.